

Discrete Iron(III) Oxide Nanoislands for Efficient and Photostable Perovskite Solar Cells

**Qiang Luo, Haijun Chen, Yuze Lin, Huayun Du, Qinzhi Hou, Feng Hao, Ning Wang,*
Zhanhu Guo,* and Jinsong Huang***

Perovskite solar cells typically use TiO_2 as charge extracting materials, which reduce the photostability of perovskite solar cells under illumination (including ultraviolet light). Simultaneously realizing the high efficiency and photostability, it is demonstrated that the rationally designed iron(III) oxide nanoisland electrodes consisting of discrete nanoislands *in situ* growth on the compact underlayer can be used as compatible and excellent electron extraction materials for perovskite solar cells. The uniquely designed iron(III) oxide electron extraction layer satisfies the good light transmittance and sufficient electron extraction ability, resulting in a promising power conversion efficiency of 18.2%. Most importantly, perovskite solar cells fabricated with iron(III) oxide show a significantly improved UV light and long-term operation stabilities compared with the widely used TiO_2 -based electron extraction material, owing to the low photocatalytic activity of iron(III) oxide. This study highlights the potential of incorporating new charge extraction materials in achieving photostable and high efficiency perovskite photovoltaic devices.

1. Introduction

Metal halide perovskite solar cells have recently become one of the more exciting energy conversion devices due to their low material and fabrication cost, scalable manufacture capability

Dr. Q. Luo, Dr. H. Chen, Dr. Q. Hou, Dr. F. Hao, Prof. N. Wang
State Key Laboratory of Electronic Thin Film and Integrated Devices
University of Electronic Science and Technology of China
Chengdu 610054, P. R. China

E-mail: wangninguestc@gmail.com

Dr. Y. Lin, Prof. J. Huang
Mechanical Engineering Department
University of Nebraska
Lincoln, NE 68588, USA
E-mail: jhuang2@unl.edu

Dr. H. Du, Prof. Z. Guo
Integrated Composites Laboratory (ICL)
Department of Chemical & Biomolecular Engineering
University of Tennessee
Knoxville, TN 37996, USA
E-mail: zguo10@utk.edu

Prof. N. Wang
State Key Laboratory of Marine Resource Utilization in South China Sea
Hainan University
Haikou 570228, P. R. China

 The ORCID identification number(s) for the author(s) of this article
can be found under <https://doi.org/10.1002/adfm.201702090>.

DOI: 10.1002/adfm.201702090

and high power conversion efficiencies.^[1–5] Since the first embodiment of perovskite solar cells reported in 2009 showing a power conversion efficiency of 3.8%,^[6] the device efficiency has been boosted up to a certified 22.1% in early 2016.^[7] At present, the highest efficiency perovskite solar cells typically employ a very thin layer of mesoporous TiO_2 (around 150 nm) in combination with a compact TiO_2 layer as electron extraction material.^[8,9] The marriage of the compact and mesoscopic scaffolds not only boosts the efficiency but also surpasses the photocurrent hysteresis, which is mainly ascribed to the mesoporous TiO_2 layer that offers a high surface area at the contact for making more favorable charge extraction, and thus inhibits the accumulation of negative ionic charges at the interface.^[10]

Although the highest efficiency obtained in mesoscopic perovskite solar cells is already higher than the commercial CIGS and CdTe thin-film photovoltaic devices, several challenges, such as stability, still remain before perovskite solar cells can successfully enter the photovoltaic market.^[11–13] Despite many endeavors have been directed at improving the long-term stability of perovskite solar cells under ambient conditions such as oxygen, moisture and heat, insufficient emphasis has been placed on dealing with the UV light stability so far.^[14] In previous studies, an obviously reduced stability of TiO_2 -based perovskite solar cells under UV light has been observed and attributed to the light-induced desorption of surface-absorbed oxygen of TiO_2 ,^[15] as well as high photocatalytic activity of TiO_2 .^[16] High UV stability is very important when devices are subject to outdoor applications, especially at high altitude region on land and space-environment where UV radiation is relatively intensive.^[17] Several methods have been proposed to enhance the UV light stability, including replacing TiO_2 with UV inactive inorganic materials such as Al_2O_3 ,^[15] inserting a buffer layer between TiO_2 and perovskite layer,^[16,18] fabricating down-shifting materials in front of the TiO_2 ,^[19] and using mesoporous SnO_2 as electron extracting material.^[20] All of the above are efficacious to a certain extent for mitigating UV-induced performance degradation, while the device efficiencies are still relatively low. To obtain high efficiency and enhanced photostability, Li and coworkers replaced the solution-processed TiO_2 compact layer with an electron beam-deposited TiO_2 film, leading to an improved device stability.^[21] The judicious

control of the deep-level hole traps in electron beam-deposited TiO_2 may induce much complexity for practical production. Very recently, Shin and coworkers reported a high efficiency perovskite solar cell by using a very promising lanthanum(La)-doped BaSnO_3 perovskite (LBSO) as electron transport materials, the solar cells fabricated with LBSO obtained significantly improved photostability compared with the mesoporous TiO_2 -based devices under AM 1.5G light illumination (including UV light).^[22] To date, most previous reported perovskite devices claiming photostability have been examined with white light emitted diodes or UV-filtered solar simulators.^[23,24] Moreover, the operational photostability evaluation was generally carried out by exposing the devices to light illumination but without continuous output traces.^[9,24] As previously reported, perovskite solar cells usually experience performance degradation after continuous operation under maximum power conditions.^[21,25] Therefore, simultaneously achieving high efficiency and excellent long term operational stability under AM 1.5G light illumination is essential and urgent in the field of perovskite photovoltaic.

Iron(III) oxide, $\alpha\text{-Fe}_2\text{O}_3$, is the most thermodynamically stable iron oxide with n-type semiconducting properties^[26] and has in particular attracted attention as an electron extraction material due to its much lower conduction band energy (≈ 0.3 eV) when compared to TiO_2 .^[27] As a stable n-type semiconductor, $\alpha\text{-Fe}_2\text{O}_3$ has a low photocatalytic activity due to its high recombination rate of electrons and holes, as well as low diffusion lengths of hole,^[27,28] which could be beneficial to enhancing the UV stability of perovskite solar cells. Unsatisfactorily, $\alpha\text{-Fe}_2\text{O}_3$ has a narrow band gap of ≈ 2.3 eV, causing parasitic light absorption in visible light region below 600 nm. Consequently, the employment of iron(III) oxide as electron extraction materials for perovskite solar cells has a fundamental

challenge: thin and planar iron(III) oxide with high transmittance usually suffers from insufficient electron extraction, while thick and mesoporous iron(III) oxide exhibiting superior electron extraction ability encounters limited light transmittance. This challenge calls for specifically designed $\alpha\text{-Fe}_2\text{O}_3$ to simultaneously realize high transmittance and sufficient electron extraction ability. Herein, we designed a novel iron(III) oxide electron extraction material, in which discrete $\alpha\text{-Fe}_2\text{O}_3$ nanoislands were in situ grown on the compact $\alpha\text{-Fe}_2\text{O}_3$ underlayer. The gap between the nanoislands ensures sufficient light transmittance utilized by perovskite absorber and the nanoislands facilitate the electron extraction from perovskite. With this design, the dilemma of light transmittance and electron extraction ability can be addressed. Perovskite solar cells fabricated with $\alpha\text{-Fe}_2\text{O}_3$ nanoislands show, compared with its planar counterparts, improved electron extraction efficiency, reduced photocurrent hysteresis and increased power conversion efficiency. Furthermore, our perovskite devices show significantly enhanced performance preservation in exposure to intensive UV light and excellent long-term photostability under AM 1.5 G illumination.

2. Results and Discussion

A solution-processed micelles method was developed to experimentally realize the fluorine-doped tin oxide (FTO) loaded $\alpha\text{-Fe}_2\text{O}_3$ nanoisland films, Figure 1a. First, iron oxide nanoparticles were formed via the hydrolysis of the hydrated ferric nitrate precursor. Nonionic surfactant, polyoxyethylene-sorbitan monooleate (commercially known as Tween-80), was subsequently added into the iron oxide nanoparticle dispersion, which will be adsorbed onto the partial surface of iron oxide

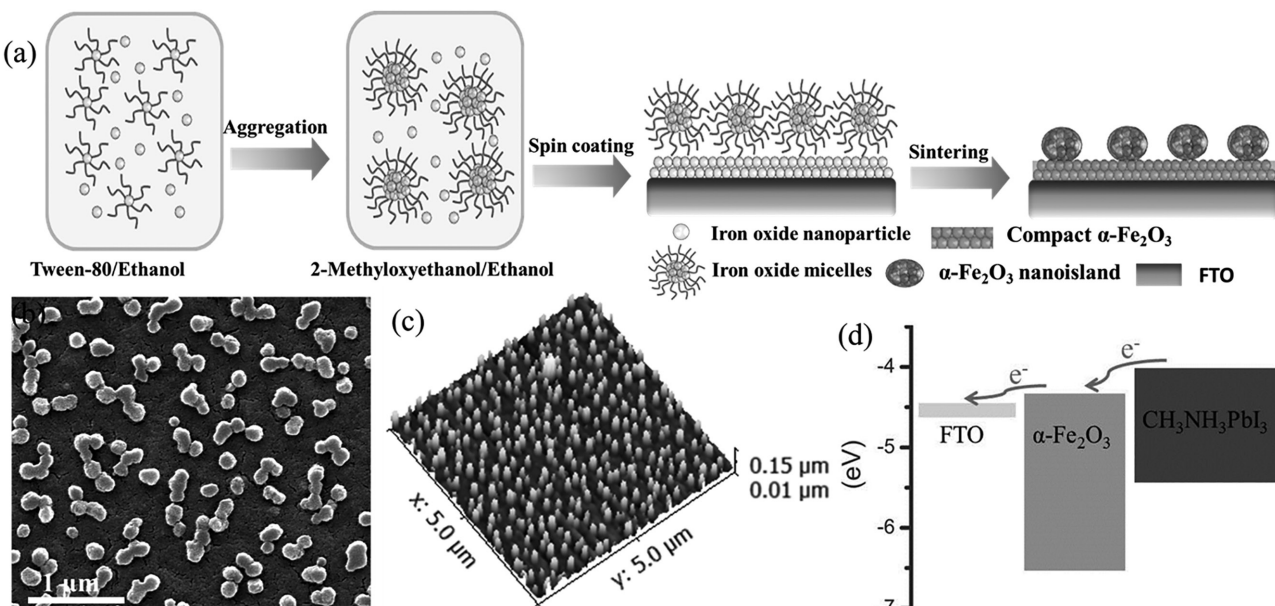


Figure 1. Synthesis and characterization of the iron(III) oxide nanoislands film. a) Schematic illustration of the preparation process of $\alpha\text{-Fe}_2\text{O}_3$ nanoislands on FTO that involves the self-aggregation of Tween-80-stabilized iron oxide into large micelles, followed by spin coating and sintering to achieve the nanoisland morphology. b) SEM images of the $\alpha\text{-Fe}_2\text{O}_3$ nanoislands film. c) AFM topography image of the $\alpha\text{-Fe}_2\text{O}_3$ nanoislands film. d) The energy level diagram of the FTO/ $\alpha\text{-Fe}_2\text{O}_3/\text{CH}_3\text{NH}_3\text{PbI}_3$ structure.

nano particles.^[29] Then, 2-methoxyethanol was incorporated into the dispersion system, which would promote the tween-iron oxide nanoparticles self-aggregation into large micelles since Tween-80 had a low solubility in 2-methoxyethanol. By spin coating, the iron oxide nanoparticles formed a compact layer on FTO substrate while the large micelles will distribute on the compact iron oxide layer. Finally, discrete $\alpha\text{-Fe}_2\text{O}_3$ nanoislands grown on compact $\alpha\text{-Fe}_2\text{O}_3$ underlayer can be obtained after removal of the Tween-80 as well as the organic moieties by combustion at 500 °C for 30 min in air atmosphere. Actually, the nanoislands films also can be obtained at a relatively low preparation temperature of 330 °C. Moreover, the discrete iron oxide nanoisland films were easily accessible and highly reproducible by the well-established spin coating technique. It should be emphasized here that both $\alpha\text{-Fe}_2\text{O}_3$ nanoisland and compact $\alpha\text{-Fe}_2\text{O}_3$ underlayer were simultaneously deposited on FTO substrate via one-step deposition method, which required a much shorter time than the conventional mesoporous TiO_2 films prepared via two-step deposition and annealing.^[4,8,30] In addition, compared with the commonly reported low-temperature process to obtain the inorganic electron extraction materials that requires complex synthesis and post-treat procedure, the fabrication process of those nanoislands films is also relatively simpler. Figure 1b shows the top-view scanning electron microscopy (SEM) image of the as-fabricated $\alpha\text{-Fe}_2\text{O}_3$ film, which demonstrates a peanut-like discrete nanoisland structure and the individual nanoisland closely grafts to the compact $\alpha\text{-Fe}_2\text{O}_3$ underlayer. As observed from the atomic force microscope (AFM) topography image in Figure 1c, the nanoislands have an average height of \approx 100 nm. The fraction of areal coverage is about 27% estimated from the large area nanoisland film (Figure S1, Supporting Information). It should be noted that the coverage of iron oxide nanoislands can be controllable depending on the amount of Tween-80 in precursor solution. For example, with the increase of Tween-80 amount from 60 to 100 mg, the coverage of nanoislands increased from \approx 27% to \approx 79% with the same spin coating speed, as shown in Figure S2 in the Supporting Information. Moreover, the size of the iron oxide nanoisland can be controlled by simply changing the spin-coating speed. It can be observed that the size of the nanoislands decreased when a relatively high spin-coating speed was used. In contrast, when a low spin-coating speed was used, smaller size was obtained as shown in Figure S3 in the Supporting Information.

The crystalline nature and identity of the $\alpha\text{-Fe}_2\text{O}_3$ film are ascertained using X-ray diffraction (XRD) (Figure S4, Supporting Information). Five diffraction peaks at 24.3, 33.3, 35.7, 49.5, and 54.5° are assigned to (012), (104), (110), (024), and (116) diffractions of $\alpha\text{-Fe}_2\text{O}_3$, respectively.^[31,32] From the Raman spectroscopy (Figure S5, Supporting Information), the observed five peaks at 224, 291, 409, 493, and 608 cm⁻¹ can be respectively assigned to the A_{1g}, E_g, E_g, A_{1g}, and E_g Raman modes for the typical $\alpha\text{-Fe}_2\text{O}_3$ phase.^[33] X-ray photoelectron spectroscopy (XPS) measurements were carried out to elucidate the chemical composition (Figure S6, Supporting Information). The XPS spectra of the Fe 2p_{3/2} peak can be separated into five distinct peaks that are consistent with previous report for $\alpha\text{-Fe}_2\text{O}_3$.^[34] The optical transmittance spectra of the as-fabricated $\alpha\text{-Fe}_2\text{O}_3$ films on FTO in the UV-visible wavelength

range are also investigated (Figure S7, Supporting Information). For comparison, compact and planar $\alpha\text{-Fe}_2\text{O}_3$ film and compact/mesoporous bilayer $\alpha\text{-Fe}_2\text{O}_3$ film were also prepared (Figure S8, Supporting Information). The planar film demonstrates high transmittance over a broad spectral range. Nevertheless, the mesoporous bilayer $\alpha\text{-Fe}_2\text{O}_3$ film shows very low transmittance value at the region between 300 and 600 nm in comparison with the planar one, which will inevitably lead to strongly parasitic light absorption in the photovoltaic devices. As expected, the nanoisland film shows a significantly higher transmittance than that of the mesoporous film in the short-wavelength region of 300–600 nm. Furthermore, a slightly higher transmittance for nanoislands film over other two samples is also observed in the region of 700–830 nm, which is due to the light scattering effect caused by nanoislands. As a consequence, this $\alpha\text{-Fe}_2\text{O}_3$ nanoislands film has a sufficient optical transparency for electron extraction layer in the photovoltaic devices.

Perovskite solar cells were then fabricated by the consecutively depositing perovskite layer, hole-transport layer, and gold electrode on the FTO loaded $\alpha\text{-Fe}_2\text{O}_3$ electron extraction layers. For comparison, planar and mesoporous $\alpha\text{-Fe}_2\text{O}_3$ perovskite solar cells were also fabricated. Figure 1d illustrates the energy level diagram of the FTO/ $\alpha\text{-Fe}_2\text{O}_3$ /perovskite structure. Upon light irradiation, the photogenerated electrons on the $\text{CH}_3\text{NH}_3\text{PbI}_3$ conduction band inject into $\alpha\text{-Fe}_2\text{O}_3$. The cross-sectional SEM images of the as-fabricated devices (planar $\alpha\text{-Fe}_2\text{O}_3$, $\alpha\text{-Fe}_2\text{O}_3$ nanoislands, and mesoporous $\alpha\text{-Fe}_2\text{O}_3$) are shown in Figure 2a. The effectiveness of these $\alpha\text{-Fe}_2\text{O}_3$ films in extracting electron from perovskite was first evaluated by performing the charge carrier dynamics (charge transfer or charge injection behavior) measurements. The steady state photoluminescence (PL) spectra of the perovskite layer spin coated on different $\alpha\text{-Fe}_2\text{O}_3$ films show a strong emission peak at around 780 nm (Figure S9, Supporting Information). The nanoislands and mesoporous $\alpha\text{-Fe}_2\text{O}_3$ loaded perovskite films showed obviously weaker emission peaks and the PL intensities were reduced by a magnitude of three-fold compared with that of planar film. This result means that the photogenerated electrons produced in perovskite can be extracted to $\alpha\text{-Fe}_2\text{O}_3$ nanoislands more quickly than planar one before bulk recombination.^[35] The electron injection process was further studied by collecting the time-resolved PL (TRPL) spectra, Figure 2b. The TRPL spectra of planar and nanoisland-based perovskite were fitted with a bi-exponential decay function containing a fast decay time constant τ_1 and a slow decay time constant τ_2 . The fast decay is attributed to the charge carrier extraction across the interface between perovskite absorber and electron extraction layer; and the slow decay comes from the radiative recombination.^[36] For the perovskite on glass substrate, the TRPL can be fitted with a single-exponential decay (Figure S10, Supporting Information). The planar electron extraction layer loaded perovskite exhibited the PL decay time up to $\tau_1 = 2.71$ ns and $\tau_2 = 21.01$ ns, obviously slower than that of pure perovskite (Table S1, Supporting Information). For nanoislands loaded perovskite, both τ_1 and τ_2 were shortened to 0.68 and 4.28 ns, respectively, and τ_2 is almost overwhelmed by τ_1 (the relative amplitude is 99.7%) and those values were comparable with the mesoporous $\alpha\text{-Fe}_2\text{O}_3$ loaded perovskite ($\tau_1 = 0.55$ ns,

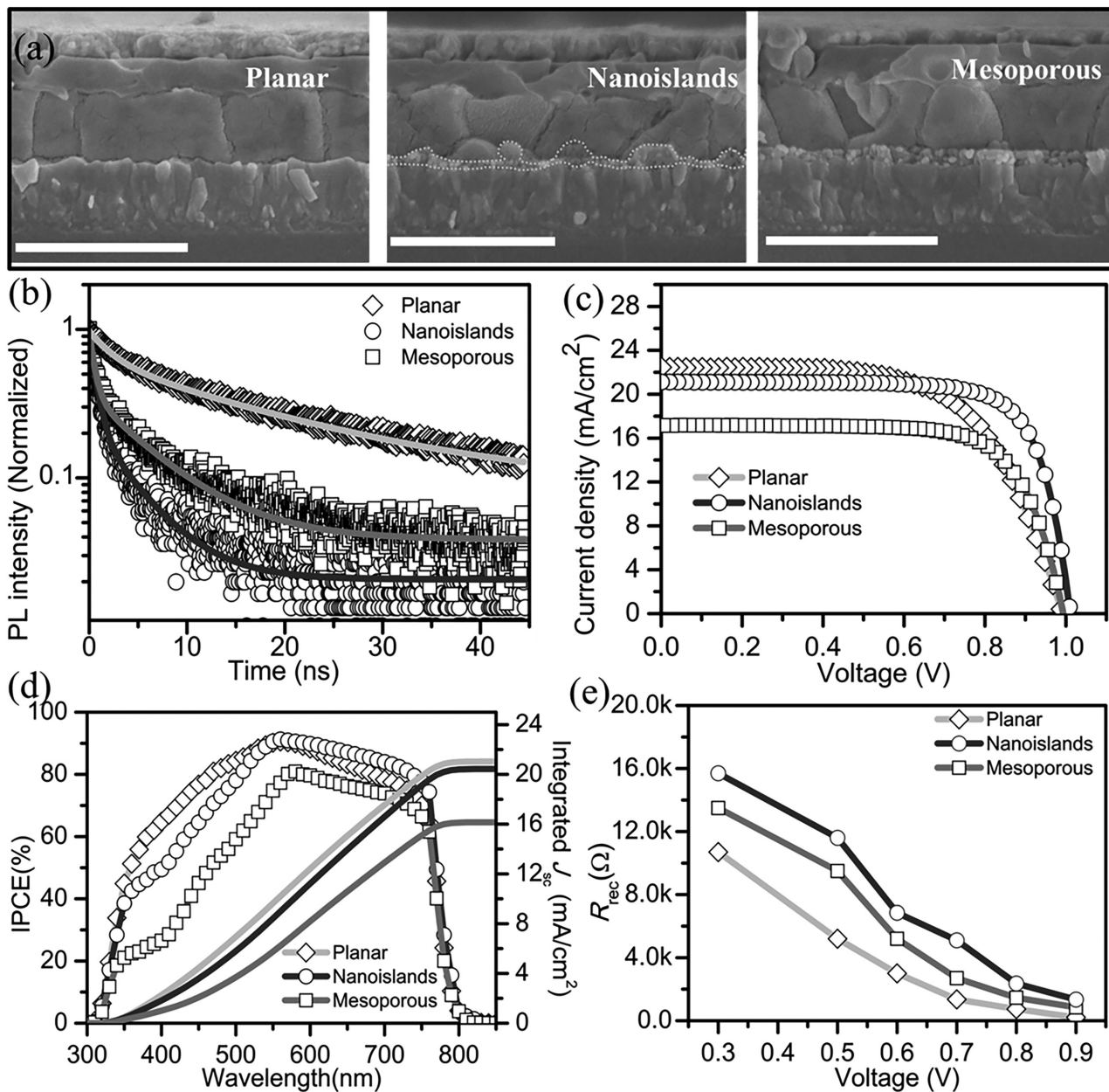


Figure 2. a) Cross-sectional SEM images of the planar $\alpha\text{-Fe}_2\text{O}_3$, $\alpha\text{-Fe}_2\text{O}_3$ nanoislands, and mesoporous $\alpha\text{-Fe}_2\text{O}_3$ devices. Scale bar, 1 μm . b) Time-resolved photoluminescence spectra of perovskite loaded on different iron(III) oxide electron extraction layers. c) $J\text{-}V$ characteristics of perovskite solar cells under AM 1.5G illumination (100 mW cm⁻²). d) IPCE spectra. e) Recombination resistance at different applied bias in dark.

$\tau_2 = 6.19$ ns), suggesting that the depopulation of photo-generated charges was dominated by charge collection through the $\alpha\text{-Fe}_2\text{O}_3$ nanoislands/perovskite interface. The improved charge collection efficiency should be mainly ascribed to the nanoislands and mesoporous $\alpha\text{-Fe}_2\text{O}_3$ films that offer higher surface areas at the contacts for making more favorable charge extraction.^[10]

Figure 2c shows three photocurrent density–voltage ($J\text{-}V$) curves for solar cells employing different electron extraction layers measured with a reverse bias scan (that is, positive bias to negative bias) under AM 1.5G illumination (100 mW cm⁻²). The corresponding photovoltaic parameters

including short-circuit current density (J_{sc}), open-circuit voltage (V_{oc}), and fill factor (FF) are summarized in Table S2 in the Supporting Information. The planar and mesoporous devices give average J_{sc} of 22.5 ± 0.96 and 17.1 ± 0.74 mA cm⁻², FF of 0.63 ± 0.03 and 0.73 ± 0.02 , and PCE of 13.9 ± 1.0 and $12.4 \pm 0.8\%$, respectively. Mesoporous devices produced increased FF but lower J_{sc} . Very encouragingly, J_{sc} of 20.9 ± 0.8 mA cm⁻², FF of 0.76 ± 0.02 , and PCE of $16.2 \pm 1.1\%$ were obtained in the case of nanoisland-based devices while the change of V_{oc} was negligible. Compared with the previously reported high efficiency mesoporous perovskite solar cells,^[9,22] solar cells with $\alpha\text{-Fe}_2\text{O}_3$ electron extracting materials generally show lower

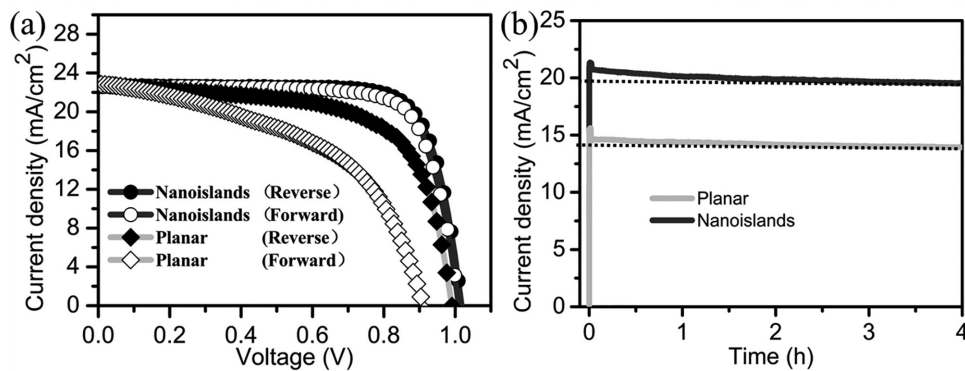


Figure 3. a) J - V curves of the top-performing solar cells under forward (from -0.1 to 1.2 V, solid) and reverse (from 1.2 to -0.1 V, open) scans. b) The stabilized photocurrent densities measured under constant bias of 0.79 V (planar device) and 0.86 V (nanoislands device) near their maximum power point.

FFs, which could be attributed to the short charges diffusion length and the high charge recombination of $\alpha\text{-Fe}_2\text{O}_3$.^[27,28] The histogram of PCEs for different solar cells are presented in Figure S11 in the Supporting Information. The PCE of nanoisland-based devices outperformed significantly the control planar and mesoporous solar cells, which is attributed to the rationally designed nanostructure. The geometry of $\alpha\text{-Fe}_2\text{O}_3$ nanoislands film has several advantages for perovskite solar cells. First, the gaps between nanoislands ensure sufficient light transmittance and the size of nanoislands enhances the light scattering effect. Second, each nanoisland is electrically connected to the compact $\alpha\text{-Fe}_2\text{O}_3$ underlayer so that all the nanoislands contribute to the efficiency. Third, the nanoislands provide large surface area contact to perovskite that ensures sufficient electron extraction. The photovoltaic performances of perovskite solar cells fabricated with different nanoisland coverage were also investigated, as shown in Table S2 (Supporting Information). It was found that solar cells with a low nanoisland coverage ($\approx 8\%$) obtained a relatively low FF of 0.69 , which may be ascribed to the insufficient electron extracting ability resulting from the low nanoisland coverage. However, perovskite solar cells with a high nanoisland coverage ($\approx 78\%$) showed a low PCE of 13.7% . In the latter case, although sufficient electron extracting ability was obtained, the parasitic absorption of iron oxide will inevitably lead to significantly decreased photocurrent density. In addition, the effect of nanoisland size on the device performance was also investigated; it was observed that the devices with different nanoisland sizes actually delivered similar PCEs. The incident photon to current efficiency (IPCE) spectra of solar cells using different $\alpha\text{-Fe}_2\text{O}_3$ were measured (Figure 2d). As shown, the mesoporous device showed an obviously lower IPCE value compared with the planar device in the wavelength region of 300 – 800 nm owing to the strongly parasitic light absorption of the thick $\alpha\text{-Fe}_2\text{O}_3$, which explained the low J_{sc} in this device. Additionally, the nanoisland-based device exhibited higher IPCE value in the long wavelength region above 600 nm than that of both planar and mesoporous devices, as a result of light scattering effect caused by nanoislands. Impedance spectroscopy (IS) was characterized to clarify the recombination behavior of our solar cells. Figure 2e shows the R_{rec} values of these three devices under different applied voltages. All the devices show a similar decrease of R_{rec} with increasing

the bias voltage due to increased carrier densities, and a higher R_{rec} value is observed in the nanoisland-based solar cell at any bias voltage in comparison with other devices, thereby indicating a slower recombination rate in this device.^[37–39]

Figure 3a presents the J - V curves of the best performing planar and nanoisland solar cells, measured at forward and reverse modes. All the extracted photovoltaic parameters are summarized in Table S3 in the Supporting Information. The planar device obviously showed severe hysteresis in the resultant J - V curves, with the PCEs of 14.8% and 10.5% measured under reverse and forward scans respectively. Very encouragingly, the nanoisland-based solar cell not only afforded more enhanced PCEs of 18.2% and 17.6% measured under reverse and forward scans but also showed negligible J - V hysteresis. The efficient electron transfer from the perovskite to the nanoisland-based film would inhibit negative ionic charge accumulation at the $\text{CH}_3\text{NH}_3\text{PbI}_3/\alpha\text{-Fe}_2\text{O}_3$ interface, which could ultimately result in a negligible hysteresis.^[38,40,41] In addition, according to recent report that perovskite suffers from ion migration during the device operation, the migration and accumulation of ions at the interface where the charges selectively contact can affect the device performances over a time scale of hours,^[25] thus it is very necessary to track the photocurrent around the maximum power point over several hours to assess the real operational performance of perovskite solar cells. Figure 3b presents the stabilized photocurrent output of planar and nanoisland-based perovskite solar cells measured under a constant bias voltage (close to the maximum power point) of 0.79 and 0.87 V, respectively. The photocurrent was stabilized to 14 and 20 mA cm^{-2} , yielding stabilized power conversion of 11.1% and 17.4% for planar and nanoisland-based perovskite solar cells, respectively. The PCE of our nanoisland-based device is higher than that of the as-reported perovskite solar cells fabricated with ZnO ,^[42] Zn_2SnO_4 ,^[43] WO_x ,^[44] and CdS ,^[45] and is also comparable with the devices fabricated with SnO_2 ,^[46,47] and organic phenyl-C61-butric acid methyl ester (PCBM).^[48]

Although continuous improvement in the performance of perovskite solar cells has been made in past several years, the UV light stability is still a critical issue for their commercial applications. The UV light stability of $\alpha\text{-Fe}_2\text{O}_3$ nanoisland-based devices was first examined under UV light illumination

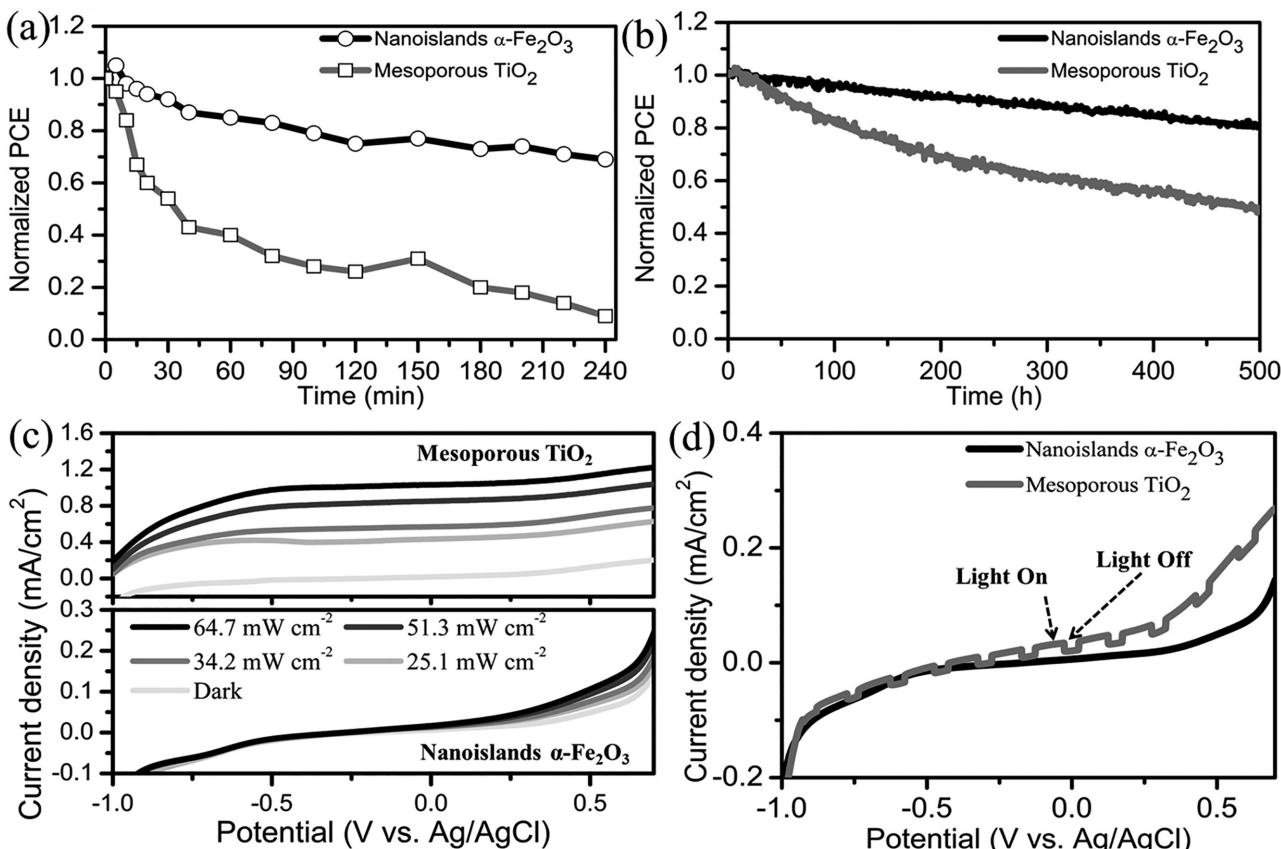


Figure 4. a) Stability of the solar cells fabricated with iron(III) oxide nanoislands (black open curve) and mesoporous TiO₂ (gray open curve) under 500 mW cm⁻² UV light illumination. b) Long-term stability of the iron(III) oxide and TiO₂-based solar cells, the curves were measured at the maximum power point voltage under AM 1.5G illumination in N₂ atmosphere and no UV filter was used. The I-V curves of the photoelectrochemical oxidation of methylamine in water using α-Fe₂O₃ nanoislands and mesoporous TiO₂ on FTO glass as photoanodes measured c) under different UV light intensities and d) under chopped simulated sunlight (AM 1.5G illumination). The anodic scan rate was 10 mV s⁻¹.

without any encapsulation. The devices were directly exposed to UV irradiation ($\lambda = 365$ nm) with an intensity of 500 mW cm⁻² in air, and the cells were removed at certain time intervals to measure the J - V curves under AM 1.5G illumination. The UV irradiation intensity used in this study was 100 times higher than that in the practical solar irradiance, which was to directly observe the discernible device performance degradation induced by UV light.^[16] For comparison, standard mesoscopic TiO₂-based devices were also fabricated adopting the device configuration of FTO/compact TiO₂/mesoporous TiO₂/CH₃NH₃PbI₃/spiro-OMeTAD/Au (PCE = 18%). As shown in Figure 4a, the TiO₂ device underwent obvious performance degradation, only 40% of its original value within the first 1 h UV illumination in air, and 10% of its original value after 4 h. In sharp contrast, the α-Fe₂O₃ device exhibited significantly improved stability, preserving 85% of its original PCE after 1 h UV light soaking and slowly degraded to about 70% after another 3 h. These solar cells with α-Fe₂O₃ nanoislands also exhibited better stability than those devices fabricated with planar α-Fe₂O₃ (Figure S12, Supporting Information), and the CsBr modified TiO₂ under similar UV irradiation (45% of the initial value after 50 min, 532 mW cm⁻²).^[16] In addition, the long-term photostability of perovskite solar cell was also evaluated by operating at the maximum power point

voltage under AM 1.5G illumination without UV filter (devices were tested in N₂ atmosphere). The TiO₂ based perovskite solar cells decay much faster than the α-Fe₂O₃ based device when subjected to AM 1.5G illumination in N₂ atmosphere, the efficiency decayed by about 51% from its initial value after continuous operation for 500 h (Figure 4b). This is in contrast to only 18% decay after 500 h illumination for the α-Fe₂O₃ based devices. Moreover, solar cells with α-Fe₂O₃ nanoislands also exhibit better stability than the planar α-Fe₂O₃ perovskite solar cells (Figure S13, Supporting Information) (35% degradation after 500 h), as well as the perovskite solar cells fabricated with the UV inactive Al₂O₃ scaffold tested under similar working conditions.^[15] The improved photostability of α-Fe₂O₃ nanoisland-based solar cells compared with the planar α-Fe₂O₃ devices could be ascribed to the enhanced light absorption of nanoisland film in the UV light region. The humidity stability of perovskite solar cells was also investigated as a function of storage time under a constant environment (relative humidity: 50%, temperature: 40 °C). Figure S14 (Supporting Information) exhibits the humidity stability of α-Fe₂O₃ based devices without encapsulation. The α-Fe₂O₃-based device retained 94% of its initial value after 600 h, whereas the TiO₂-based perovskite solar cells degraded to 73% of its initial PCE within 600 h. Those results suggest that employing α-Fe₂O₃ nanoislands as

the electron extracting layer is an effective way to enhance the stability of perovskite solar cells.

The compositional analysis on perovskite may shed light on tracing the source for the improved light stability. The α -Fe₂O₃ nanoislands and mesoporous TiO₂ loaded perovskite films before and after UV irradiation were examined by XRD shown (Figure S15, Supporting Information). The fresh perovskite films deposited on α -Fe₂O₃ and TiO₂ substrates showed tetragonal CH₃NH₃PbI₃ characteristic peaks and similar crystallinity. After 1 h UV illumination, the most obvious change of the TiO₂ loaded perovskite was the appearance of a new PbI₂ peak of (001) face at 12.5° and the peak intensity turned to be obviously higher after 4 h, indicating that the perovskite experienced decomposition in the mesoporous TiO₂ films upon UV light irradiation and the process occurred more severely with the extension of exposure time. In the case of α -Fe₂O₃ loaded perovskite, only very weak PbI₂ peak was observed after 4 h UV light soaking. Those changes were also confirmed by UV-vis measurements (Figure S16, Supporting Information). Without the UV illumination, the TiO₂-loaded perovskite exhibited strong absorption in the visible range from 480 to 770 nm, whereas after 4 h the absorption intensity dropped dramatically coupled with an additional PbI₂ absorption threshold shoulder located at around 520 nm. The resultant PbI₂ produced at the interface between perovskite and TiO₂ will hinder the electron transfer from perovskite to TiO₂, leading to lower device efficiency.^[16] In contrast, the α -Fe₂O₃ loaded perovskite film exhibited little absorption loss even after 4 h UV exposure, which was consistent with the unchanged XRD patterns. In addition, the UV light induced morphological changes in the films were also investigated (Figure S17, Supporting Information). Before UV exposure, the α -Fe₂O₃ and TiO₂ loaded perovskite films have similar film morphology with clear grain boundary. However, after 2 h UV aging, the perovskite film on the TiO₂ substrate has been changed obviously and the grain boundaries become indistinguishable. It is also worth noting that many pinholes appeared in TiO₂ loaded perovskite film after UV light aging, which could be ascribed to the evaporation of CH₃NH₂ (b. p. 17 °C) from the perovskite film owing to UV induced degradation of CH₃NH₃PbI₃.^[18,49] However, the morphology for the perovskite films processed upon the α -Fe₂O₃ substrate did not change noticeably after UV aging. The above results clearly show the enhanced stability of α -Fe₂O₃-based solar cells in comparison with TiO₂-based devices.

To understand the mechanism of performance degradation induced by UV and AM 1.5G light soaking, the photocatalytic activity of the as-fabricated α -Fe₂O₃ nanoislands and mesoporous TiO₂ films was evaluated by photoelectrochemical oxidation of methylamine (CH₃NH₂) in aqueous solution.^[21] The dark current and photocurrent are shown as a function of bias applied at the FTO loaded oxide electrodes in Figure 4c. As shown, the photocurrent of the mesoporous TiO₂ thin film increased with the increase of UV light intensity, and was significantly higher than that of the α -Fe₂O₃ thin film. The α -Fe₂O₃ thin film showed low photocurrent even at a high UV light intensity of 63 mW cm⁻², which was also obviously lower than that of planar TiO₂ sample (Figure S18, Supporting Information). The photocatalytic activity of this α -Fe₂O₃ thin film was also examined under AM 1.5 G illumination (Figure 4d). The

mesoporous TiO₂ thin film exhibited obvious photoresponse in AM 1.5 G illumination whereas the photoresponse for α -Fe₂O₃ nanoislands films was negligible. Those results clearly indicate the lower photocatalytic activity of our α -Fe₂O₃ compared with the TiO₂ electron extraction material, which could be ascribed to the high recombination rate of electrons and holes, as well as low diffusion lengths of the holes in α -Fe₂O₃ film.^[26,28] The lower photocatalytic activity of the α -Fe₂O₃ leads to a more benign material interface between the perovskite and α -Fe₂O₃ and thus increases the stability of the perovskite solar cells.^[16,21]

3. Conclusion

A unique α -Fe₂O₃ nanoisland structure had been successfully designed to apply as electron extraction materials for high-performance perovskite solar cells. This novel design simultaneously afforded good transmittance and sufficient electron extraction ability. Perovskite solar cells fabricated with α -Fe₂O₃ nanoislands showed, compared with the planar α -Fe₂O₃ electrode, improved electron extraction, reduced charge recombination, increased PCE, and negligible J-V hysteresis. More importantly, the UV light stability of the devices was significantly improved compared with the TiO₂-based devices due to the low photocatalytic α -Fe₂O₃. This materials' design for perovskite solar cells could also be extended to other charge extraction materials that suffer from light transmittance issue but own excellent electron extraction ability and low photocatalytic activity, considering the increasing efforts dedicated to developing more stable perovskite photovoltaic devices.

4. Experimental Section

Preparation of the Iron(III) Oxide Electron Extraction Layers: The FTO-coated glass substrates were ultrasonically washed with detergent, deionized water, ethanol, acetone, and isopropanol for 15 min successively. The cleaned FTO glass was treated with an ultraviolet/O₃ cleaner for at least 15 min. Polysorbate-80 (Tween 80) polymer with an average molecular weight of 79 000 g mol⁻¹ and a density of 1.06 g cm⁻³ was purchased from Sigma-Aldrich. In a water-free container, 110 mg Fe(NO₃)₃·9H₂O dissolved in 2 mL ethanol solution, followed by the addition of 60 mg polysorbate-80. The mixed solution was stirred at 600 rpm for 30 min. Then 0.6 mL 2-methoxyethanol was added to the above ethanol solution and the solution was stirred at 600 rpm for another 30 min. The precursor was spin-coated on cleaned FTO substrates at 6000 rpm for 40 s (acceleration speed 1000 rpm s⁻¹). Optimal relative humidity was 50–70%. The films were left in air for 30 min and then were heated to 250 °C using 4 h ramp and aged at this temperature for 12 h. Thereafter, the samples were heated to 500 °C in an oxygen atmosphere using 60 min ramp and were annealed at 500 °C for 30 min.

For the preparation of the compact and planar iron(III) oxide film, 0.05 M Fe(NO₃)₃·9H₂O dissolved in ethanol was spun on the cleaned FTO glass at 6000 rpm for 40 s, followed by sintering at 500 °C for 30 min in air. The compact/mesoporous α -Fe₂O₃ film was prepared by spin coating the α -Fe₂O₃ nanoisland precursor (the dosage of polysorbate-80 is 160 mg) onto the planar α -Fe₂O₃ film at 4000 rpm for 40 s. The films were heated to 500 °C in an oxygen atmosphere using 5 h ramp and are annealed at 500 °C for 30 min.

Device Fabrication: The perovskite precursor solution was prepared by dissolving PbI₂ and CH₃NH₃I into the solvent of dimethyl sulfoxide and N,N-dimethylformamide (3:7 volume ratio), followed by stirring at

room temperature for 4 h to produce a clear solution. Subsequently, in an N₂-purged glove box (<1.0 ppm O₂ and H₂O), the perovskite precursor solution was coated onto the iron(III) oxides coated FTO substrate by two consecutive spin-coating steps of 1000 and 3500 rpm for 15 and 40 s, respectively. 500 μL toluene was rapidly dropped on the substrates to induce fast crystallization after 30 s spin-coating. To remove excess reagents or solvent, the preliminary perovskite film was immediately placed on a hot plate at 100 °C for 25 min. The thickness of the perovskite layer was about 520 nm. After the films were cooled down to room temperature, the hole-transporting material (HTM) was subsequently spin cast on perovskite layer by spin coating a mixture solution (4000 rpm for 40 s), which was prepared by adding 72.3 mg 2,2',7,-7'-tetrakis(*N,N*-di-p-methoxyphenylamine)-9,9'-spirobifluorene (spiro-OMeTAD), 28.8 μL 4-tert-butylpyridine, and 17.5 μL stock solution consisting of 520 mg mL⁻¹ lithium bis(trifluoromethylsulphonyl)imide in acetonitrile to 1 mL chlorobenzene. Finally, Au electrode was deposited on the HTM layer by thermal evaporation. The fabricated devices were left in a drying air for 12 h before test.

For the fabrication of the mesoporous TiO₂ solar cells, a compact TiO₂ layer was first prepared by spin-coating an acidic solution of titanium isopropoxide in anhydrous ethanol on cleaned FTO substrates, followed by sintering at 500 °C for 30 min. The TiO₂ mesoporous layer was subsequently deposited on the compact layer by spin-coating a colloidal dispersion of TiO₂ at 5000 rpm, and then sintering at 500 °C for 30 min. The process of fabricating perovskite layer, HTM layer, and Au back electrode on TiO₂ substrates is similar to the α-Fe₂O₃-based solar cells.

Material and Device Characterization: The XRD patterns were obtained using a Bruker D8 Advance diffractometer with Cu K α at a voltage of 40 kV and a current of 40 mA ($\lambda = 1.5406 \text{ \AA}$). The microstructure of samples was characterized with scanning electron microscope (SEM, LEO 1530, Gemini, Zeiss, Germany). The AFM investigations were carried out on asylum research cypher (Cypher S, Oxford Instruments) microscopes. The steady-state PL emission spectra and TRPL decay spectra were measured by using a fluorescence spectrometer instrument (FLS920, Edinburgh Instruments, Livingston, UK). A picosecond pulsed diode laser with excitation wavelength of 405 nm was available to record the emission decay curves. A 450 W ozone-free xenon lamp was used for steady-state PL measurements. Photoelectrochemical properties of the α-Fe₂O₃ and TiO₂ thin films were measured in a three-electrode configuration, with a Ag/AgCl and a Pt wire as reference electrode and counter electrode, respectively. An aqueous solution containing 1 wt% methylamine was used as the electrolyte. The current–voltage (I–V) curves were measured under chopped simulated sunlight (AM 1.5G irradiation, 100 mW cm⁻²) and anodic scan at a rate of 10 mV s⁻¹. For photoelectrochemical reactions performed under UV light, the UV light was generated from a high-voltage mercury lamp. The intensity of the incident UV beam was determined by a radiometer (FA-Z, Photoelectric Instrument Factory of Beijing Normal University, China).

The photocurrent density–voltage (J–V) characteristics of the perovskite devices were measured by utilizing a digital source meter (2401, Keithley Instruments, USA) under AM 1.5G irradiation (100 mW cm⁻²), which was realized by a solar simulator (91192, Oriel, USA) and calibrated by a standard silicon solar cell before measurement. The incident photon to current efficiency (IPCE) was recorded by using a solar cell quantum efficiency measurement system (QEX10, PV measurements, USA). IS measurements were performed by using the Zahner system (Zahner, Zahner-Elektrik GmbH&Co.KG, Germany) and the Z-view software was used to analyze the impedance data. The UV irradiation for solar cells was provided by UV resource (Intelli-RAY 400).

Supporting Information

Supporting Information is available from the Wiley Online Library or from the author.

Acknowledgements

This work was supported by the China–Japan International Cooperation Program Funds (Nos. 2010DFA61410 and 2011DFA50530), the National Natural Science Foundations of China (Nos. 51272037, 51272126, 51303116, and 51472043) and Program for New Century Excellent Talents in University (No. NCET-12-0097).

Conflict of Interest

The authors declare no conflict of interest.

Keywords

electron extracting materials, iron(III) oxides, perovskite solar cells, photostability

Received: April 19, 2017

Revised: June 5, 2017

Published online:

- [1] M. M. Lee, J. Teuscher, T. Miyasaka, T. N. Murakami, H. J. Snaith, *Science* **2012**, *338*, 643.
- [2] H. Kim, C. Lee, J. Im, K. Lee, T. Moehl, A. Marchioro, S. Moon, R. Humphry-Baker, J. Yum, J. E. Moser, M. Gratzel, N. Park, *Sci. Rep.* **2012**, *2*, 591.
- [3] J. Burschka, N. Pellet, S. Moon, R. Humphry-Baker, P. Gao, M. K. Nazeeruddin, M. Gratzel, *Nature* **2013**, *499*, 316.
- [4] N. J. Jeon, J. H. Noh, W. S. Yang, Y. C. Kin, S. Ryn, J. Seo, S. I. Seok, *Nature* **2015**, *517*, 476.
- [5] H. Zhou, Q. Chen, G. Li, S. Luo, T. Song, H. Duan, Z. Hong, J. You, Y. Liu, Y. Yang, *Science* **2014**, *345*, 542.
- [6] A. Kojima, K. Teshima, Y. Shirai, T. Miyasaka, *J. Am. Chem. Soc.* **2009**, *131*, 6050.
- [7] National Renewable Energy Laboratory, Best Research-Cell Efficiencies chart, www.nrel.gov/ncpv/images/efficiency_chart.jpg, accessed July, 2017.
- [8] M. Saliba, T. Matsui, J. Seo, K. Domanski, J. Correa-Baena, M. K. Nazeeruddin, W. Tress, A. Abate, A. Hagfeldt, M. Gratzel, *Energy Environ. Sci.* **2016**, *9*, 1989.
- [9] M. Saliba, T. Matsui, K. Domanski, J. Seo, A. Ummadisingu, S. K. Zakeeruddin, J. Correa-Baena, W. R. Tress, A. Abate, A. Hagfeldt, M. Gratzel, *Science* **2016**, *354*, 206.
- [10] W. Zhang, G. E. Eperon, H. J. Snaith, *Nat. Energy* **2016**, *1*, 16048.
- [11] N. G. Park, M. Grätzel, T. Miyasaka, K. Zhu, K. Emery, *Nat. Energy* **2016**, *1*, 16152.
- [12] A. Babayigit, A. Ethirajan, M. Muller, B. Conings, *Nat. Mater.* **2016**, *15*, 247.
- [13] E. J. Juarez-Perez, Z. Hawash, S. R. Raga, L. K. Ono, Y. Qi, *Energy Environ. Sci.* **2016**, *9*, 3406.
- [14] T. Leijtens, G. E. Eperon, N. K. Noel, S. N. Haberreuter, A. Petrozza, H. J. Snaith, *Adv. Energy Mater.* **2015**, *5*, 1500963.
- [15] T. Leijtens, G. E. Eperon, S. Pathak, A. Abate, M. M. Lee, H. J. Snaith, *Nat. Commun.* **2013**, *4*, 2885.
- [16] W. Li, W. Zhang, S. V. Reenen, R. J. Sutton, J. Fan, A. A. Haghighirad, M. B. Johnston, L. Wang, H. J. Snaith, *Energy Environ. Sci.* **2016**, *9*, 490.
- [17] Y. Zhou, K. Zhu, *ACS Energy Lett.* **2016**, *1*, 64.
- [18] S. Ito, S. Tanaka, K. Manabe, H. Nishino, *J. Phys. Chem. C* **2014**, *118*, 16995.

- [19] N. Chander, A. F. Khan, P. S. Chandrasekhar, E. Thouti, S. K. Swami, V. Dutta, V. K. Komarala, *Appl. Phys. Lett.* **2014**, *105*, 033904.
- [20] B. Roose, J. C. Baena, K. C. Godel, M. Graetzel, A. Hagfeldt, U. Steiner, A. Abate, *Nano Energy* **2016**, *30*, 517.
- [21] Y. Li, J. K. Cooper, W. Liu, C. M. Sutter-Fella, M. Amani, J. W. Beeman, A. Javey, J. W. Ager, Y. Liu, F. M. Toma, I. D. Sharp, *Nat. Commun.* **2016**, *7*, 12446.
- [22] S. S. Shin, E. L. Yeom, W. S. Yang, S. Hur, M. G. Kim, J. Im, J. Seo, J. H. Noh, S. Seok, *Science* **2017**, *356*, 167.
- [23] M. Saliba, T. Matsui, J. Y. Seo, K. Domanski, J. P. Correa-Baena, M. K. Nazeeruddin, S. M. Zakeeruddin, W. Tress, A. Abate, A. Hagfeldt, M. Grätzel, *Energy Environ. Sci.* **2016**, *9*, 1989.
- [24] W. Chen, Y. Wu, Y. Yue, J. Liu, W. Zhang, X. Yang, H. Chen, E. Bi, I. Ashraful, M. Grätzel, L. Han, *Science* **2015**, *350*, 944.
- [25] K. Domanski, B. Roose, T. Matsui, M. Saliba, S. Turren-Cruz, J. Correa-Baena, C. R. Carmona, G. Richardson, J. M. Foster, F. D. Angelis, J. M. Ball, A. Petrozza, N. Mine, M. K. Nazeeruddin, W. Tress, M. Grätzel, U. Steiner, A. Hagfeldt, A. Abate, *Energy Environ. Sci.* **2017**, *10*, 604.
- [26] K. Sivula, F. Le Formal, M. Grätzel, *ChemSusChem* **2011**, *4*, 432.
- [27] M. Grätzel, *Nature* **2001**, *414*, 338.
- [28] M. J. Katz, S. C. Riha, N. C. Jeong, A. B. F. Martinson, O. K. Farha, J. T. Hupp, *Coord. Chem. Rev.* **2012**, *256*, 2521.
- [29] R. Xu, H. Zeng, *Langmuir* **2004**, *20*, 9780.
- [30] Z. Sun, L. Zhang, F. Dang, Y. Liu, Z. Fei, Q. Shao, H. Lin, J. Guo, L. Xiang, N. Yerra, Z. Guo, *CrystEngComm* **2017**, *19*, 3288.
- [31] Z. Sun, H. Yuan, Z. Liu, B. Han, X. Zhang, *Adv. Mater.* **2005**, *17*, 2993.
- [32] W. Hu, T. Liu, X. Yin, H. Liu, X. Zhao, S. Luo, Y. Guo, Z. Yao, J. Wang, N. Wang, Z. Guo, *J. Mater. Chem. A* **2017**, *5*, 1434.
- [33] D. L. A. de Faria, S. Venancio Silva, M. T. de Oliveira, *J. Raman Spectrosc.* **1997**, *28*, 873.
- [34] A. P. Grosvenor, B. A. Kobe, M. C. Biesinger, N. S. McIntyre, *Surf. Interface Anal.* **2004**, *36*, 1564.
- [35] Y. Hou, O. R. Quiroz, S. Scheiner, W. Chen, T. Stubhan, A. Hirsch, M. Halik, C. J. Brabec, *Adv. Energy Mater.* **2015**, *5*, 1501056.
- [36] Y. Li, Y. Zhao, Q. Chen, Y. Yang, Y. Liu, Z. Hong, Z. Liu, Y. Hsieh, L. Meng, Y. Li, Y. Yang, *J. Am. Chem. Soc.* **2015**, *137*, 15540.
- [37] L. Liu, A. Mei, T. Liu, P. Jiang, Y. Sheng, L. Zhang, H. Han, *J. Am. Chem. Soc.* **2015**, *137*, 1790.
- [38] Q. Luo, H. Ma, Y. Zhang, X. Yin, Z. Yao, N. Wang, J. Li, A. Fan, K. Jiang, H. Lin, *J. Mater. Chem. A* **2016**, *4*, 5569.
- [39] E. J. Juarez-Perez, M. Wular, F. Fabregat-Santiago, K. Lakus-Wollny, E. Mankel, T. Mayer, W. Jaegermann, I. Mora-Sero, *J. Phys. Chem. Lett.* **2014**, *5*, 680.
- [40] H. Kim, I. Jang, N. Ahn, M. Choi, A. Guerrero, J. Bisquert, N. Park, *J. Phys. Chem. Lett.* **2015**, *6*, 4633.
- [41] B. Wu, K. Fu, N. Yantara, G. Xing, S. Sun, T. C. Sum, N. Mathews, *Adv. Energy Mater.* **2015**, *5*, 1500829.
- [42] D. Liu, T. L. Kelly, *Nat. Photonics* **2014**, *8*, 133.
- [43] S. S. Shin, W. S. Yang, J. H. Noh, J. H. Suk, N. J. Jeon, J. H. Park, J. S. Kim, W. M. Seong, S. Sang, *Nat. Commun.* **2015**, *6*, 7410.
- [44] K. Wang, Y. Shi, B. Li, L. Zhao, W. Wang, X. Wang, X. Bai, S. Wang, C. Hao, T. Ma, *Adv. Mater.* **2016**, *9*, 1891.
- [45] I. Hwang, K. Yong, *ACS Appl. Mater. Interfaces* **2016**, *8*, 4226.
- [46] J. P. C. Baena, L. Steier, W. Tress, M. Saliba, S. Neutzner, T. Matsui, F. Giordana, T. J. Jacobsson, A. R. S. Kandada, S. M. Zakeeruddin, A. Petrozza, A. Abate, M. K. Nazeeruddin, M. Cratzel, A. Hagfeldt, *Energy Environ. Sci.* **2015**, *8*, 2928.
- [47] W. Ke, G. Fang, Q. Liu, L. Xiong, P. Qin, H. Tao, J. Wang, H. Lei, B. Li, J. Wan, G. Yang, Y. Yan, *J. Am. Chem. Soc.* **2015**, *137*, 6730.
- [48] J. H. Heo, H. J. Han, D. Kim, T. K. Ahn, S. H. Im, *Energy Environ. Sci.* **2015**, *8*, 1602.
- [49] G. Niu, X. Guo, L. Wang, *J. Mater. Chem. A* **2015**, *3*, 8970.